Numerical investigation of fracture interface waves

Boliang Gu, Kurt T. Nihei, and Larry R. Myer

Earth Sciences Division, Lawrence Berkeley National Laboratory, One Cyclotron Road, MS 90-1116, Berkeley, California 94720

Two-dimensional boundary element simulations are conducted to investigate the properties of Rayleigh-type fracture interface waves generated by a line source located near a single fracture. The fracture is modeled as a displacement–discontinuity boundary condition between two elastic half-spaces with identical properties. Numerical simulations are performed for different fracture stiffnesses, source polarizations, and source depths. Symmetric and antisymmetric fracture interface waves are observed with amplitudes and velocities that are controlled by the ratio of the fracture impedance to the half-space shear wave impedance, as predicted by plane-wave theory [Gu *et al.*, J. Geophys. Res. **101**, 827–835 (1996); Pyrak-Nolte and Cook, Geophys. Res. Lett. **14**, 1107–1110 (1987)]. When the source is located off the fracture, these waves develop at incidence angles that decrease with source depth. [S0001-4966(97)02207-8]

PACS numbers: 43.20.Gp, 43.20.Jr [JEG]

INTRODUCTION

Fractures in brittle materials such as rock and concrete are typically surfaces of irregular topography. Small amounts of relative motion between these surfaces can produce imperfect contact. Imperfect contact between the surfaces results in a thin, compliant interface of negligible thickness and density. Investigators in the fields of nondestructive evaluation and geophysics[1-4] have recognized that this additional compliance results in jumps in the normal and tangential displacements across the fracture that are proportional to the applied stress and compliance of the fracture. This work has established that the linear constitutive relations for a fracture can be described by a displacement–discontinuity boundary condition provided that the wavelength is long relative to the spacing between asperities of contact within the fracture.

Recent theoretical and experimental research has demonstrated that a single nonwelded interface, such as a fracture or an imperfect bond, can support Rayleigh-type interface waves which propagate along the fracture.[5-9] The amplitudes and velocities of these interface waves are sensitive to the magnitude of the shear and normal stiffnesses of the nonwelded interface, making these waves potentially useful for applications involving interface characterization.

Murty[7] examined the conditions for the existence of interface waves on a nonwelded interface with a discontinuity in the shear displacement across the interface. Pyrak-Nolte and Cook[6] extended Murty's analysis to the case where both normal and shear displacements are discontinuous across a nonwelded interface. Gu *et al.*[5] demonstrated that simple, closed-form dispersion equations for interface waves propagating along a single fracture could be obtained from the matrix equation developed by Pyrak-Nolte and Cook.[6] The basic form of these dispersion equations is similar to the classic Rayleigh equation for a surface wave on a half-space except that the symmetric and antisymmetric fracture interface waves are controlled by the fracture impedance ratio (i.e., ratio of the fracture impedance to the half-space shear

wave impedance). For low values of the fracture impedance ratio, the dispersion equations for the symmetric and antisymmetric fracture interface waves degenerate to the classic nondispersive equation for Rayleigh waves on a half-space. For large values of the fracture impedance ratio, the symmetric wave reaches a cutoff value and ceases to exist as a normal mode, while the antisymmetric wave degenerates to a shear body wave propagating along the fracture. For intermediate values of the fracture impedance ratio, both waves are dispersive with the symmetric wave propagating faster than the antisymmetric wave for a given value of the fracture impedance ratio.

While the plane-wave analysis successfully predicts the velocities of fracture interface waves observed in laboratory measurements on fractures,[8] it does not provide information about the generation of these waves by a spatially localized source. In this paper, the generation of fracture interface waves from a line source is investigated using the boundary element method. The paper begins with a brief discussion of the boundary element method formulation for an elastic medium containing a single fracture. The following section describes techniques for generating symmetric and antisymmetric fracture interface waves and evaluates the effects of the fracture impedance ratio on wave amplitudes and velocities. The final section investigates the influence of source distance from the fracture on the generation of fracture interface waves.

I. BOUNDARY ELEMENT METHOD FOR FRACTURED MEDIA

The boundary element method is an accurate and computationally efficient numerical technique for modeling elastic wave propagation in a medium containing fractures.[10] Unlike the finite element and finite difference methods, which employ space-filling numerical meshes, the boundary element method only requires discretization of the fracture and employs the fundamental point source solution. Conse-

120   J. Acoust. Soc. Am. **102** (1), July 1997

120

quently, the boundary element method is less susceptible to numerical dispersion for wave propagation problems.

An efficient two-dimensional boundary integral equation is developed by numerical integration of the three-dimensional boundary integral equations along the axis orthogonal to the plane of interest. The advantages of this approach are that the coefficient matrix for only the first time step needs to be assembled and solved, and that singularities of the Green's functions can be significantly reduced.[10,11]

For problems with zero initial conditions, the time-domain form of the three-dimensional boundary integral equation may be written as[11]

$$c_{ij}(\xi)u_i(\xi,t) = \int_{\Gamma} \{G_{ij}*\tau_i(\mathbf{x},t) - F_{ij}*u_i(\mathbf{x},t)\}d\Gamma$$

$$+ \rho \int_{\Omega} G_{ij}*b_i(\mathbf{x},t)d\Omega, \qquad (1)$$

where $u_i(\xi,t)$ is the i component of the particle displacement observed at location ξ, $u_i(\mathbf{x},t)$ and $\tau_i(\mathbf{x},t)$ are the i component of the displacement and traction on the fracture surface Γ, G_{ij} is the three-dimensional Green's function for an unbounded elastic medium, F_{ij} is the traction derived from G_{ij} using Hooke's Law, $b_i(\mathbf{x},t)$ is a volumetric source acting in volume Ω, $*$ is the time convolution operator, c_{ij} is the *free-term* resulting from the singularity of F_{ij} as $\xi \to \mathbf{x}$, and $i, j = 1,2$ for in-plane problems.

To solve the boundary integral equation for boundary displacements and tractions, the fracture surfaces are divided into boundary elements and the boundary variables are discretized in both the space and time. The discretization here is completed using quadratic shape functions and the Heaviside function for the spatial coordinate along the fracture,

$$x_i = M_\alpha X_{i\alpha}, \qquad (2)$$

and the displacement and traction along the fracture,[11]

$$u_i(\xi,t) = \sum_{n=1}^{N} M_\alpha U_{i\alpha}^n \Phi^n(t),$$

$$\qquad (3)$$

$$\tau_i(\xi,t) = \sum_{n=1}^{N} M_\alpha T_{i\alpha}^n \Phi^n(t),$$

where $X_{i\alpha}$ is the nodal coordinate of the element, $U_{i\alpha}^n$ and $T_{i\alpha}^n$ are the nodal displacement and traction, respectively, M_α is a quadratic shape function, $\Phi^n(t) = H[t-(n-1)\Delta t] - H[t-n\Delta t]$, where $H[\cdot]$ is the Heaviside function, $n = 1,2,3,\dots,N$ is the time step, and $\alpha = 1, 2$, and 3 represents the nodal points on a single boundary element.

In the numerical model, the fracture is modeled as a displacement–discontinuity boundary condition between two elastic half-spaces.[2] Across such a discontinuity, stresses are continuous and particle displacements are discontinuous. For in-plane motion, the displacement–discontinuity boundary conditions are

$$u_i^a - u_i^b = \tau_{i2}^a/k_i, \quad \tau_{i2}^a = \tau_{i2}^b, \qquad (4)$$

where superscripts a and b denote the half-space above and below the fracture, respectively, k_i is the fracture stiffness in

halfspace a

upper surface

x_2
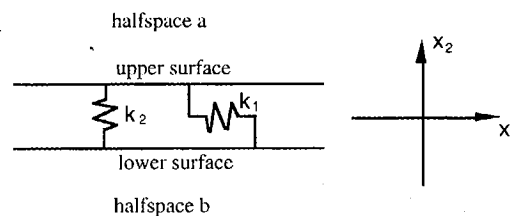
k_2 k_1

x_1

lower surface

halfspace b

FIG. 1. Displacement–discontinuity fracture model. k_1 and k_2 are the tangential and normal fracture stiffnesses.

the i direction, and $i = 1,2$ (see Fig. 1). As $k_i \to \infty$, the interface becomes welded and the particle displacements across the fracture are continuous. As $k_i \to 0$, the two surfaces of the fracture become two traction-free surfaces.

For elastic wave transmission across a single natural fracture in granite, the ultrasonic measurements of Pyrak-Nolte et al.[3] were found to exhibit frequency-dependent amplitude reductions that are well predicted by plane-wave transmission coefficients derived using the displacement-discontinuity boundary conditions given in Eq. (4). The displacement–discontinuity model has also been used extensively by researchers in nondestructive evaluation of welds and adhesive bonds[4] with considerable success.

The boundary integral equation given in Eq. (1) can be assembled to form a system of the discretized boundary integral equations for a medium containing a fracture using Eqs. (1), (2), and (3) and applying the displacement-discontinuity boundary condition of Eq. (4). The resulting linear system of such discretized equations has the following form:[10]

$$
\begin{bmatrix}
F_{11}^a + k_1 G_{11}^a & F_{12}^a + k_2 G_{12}^a & -k_1 G_{11}^a & -k_2 G_{12}^a \\
F_{21}^a + k_1 G_{21}^a & F_{22}^a + k_2 G_{22}^a & -k_1 G_{21}^a & -k_2 G_{22}^a \\
-k_1 G_{11}^b & -k_2 G_{12}^b & F_{11}^b + k_1 G_{11}^b & F_{12}^b + k_2 G_{12}^b \\
-k_1 G_{21}^b & -k_2 G_{22}^b & F_{21}^b + k_1 G_{21}^b & F_{22}^b + k_2 G_{22}^b
\end{bmatrix}
$$

$$
\times \begin{Bmatrix} U_1^a \\ U_2^a \\ U_1^b \\ U_2^b \end{Bmatrix}^n = \begin{Bmatrix} B_1^a \\ B_2^a \\ B_1^b \\ B_2^b \end{Bmatrix}^n, \qquad (5)
$$

where $\{B\}^n$ is the accumulated boundary displacements from time step 1 to $n-1$, and $[\cdot]^1$ is the coefficient matrix for the first time step. Since all quantities in $\{B\}^n$ and $[\cdot]^1$ are known, the displacements $\{U\}^n$ on the fracture surfaces at a time step n can be obtained by the numerical solution of Eq. (5). Interior displacements can be obtained by direct numerical integration of Eq. (1) once the displacements and tractions on the surfaces of the fracture are known.

II. FRACTURE INTERFACE WAVES

The analyses of Pyrak-Nolte and Cook[6] and Gu et al.[5] and laboratory measurements of Pyrak-Nolte et al.[8] demonstrate that a fracture can support dispersive symmetric (i.e., extensional mode) and antisymmetric (i.e., flexural mode) interface waves that propagate between the Rayleigh wave
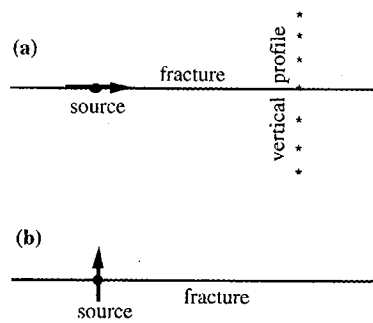
FIG. 2. Simulation geometry used to generate (a) symmetric and (b) antisymmetric fracture interface waves.

FIG. 3. Schematic illustration of the particle displacements of the symmetric and antisymmetric fracture interface waves.

and shear wave velocities. The dispersion equations for symmetric and antisymmetric fracture interface waves (Fig. 3) are[5]

$$(1-2\xi^2)^2-4\xi^2\sqrt{\xi^2-\zeta^2}\sqrt{\xi^2-1}-2\bar{k}_2\sqrt{\xi^2-\zeta^2}$$
$$=0, \quad \text{symmetric wave} \tag{6}$$

$$(1-2\xi^2)^2-4\xi^2\sqrt{\xi^2-\zeta^2}\sqrt{\xi^2-1}-2\bar{k}_1\sqrt{\xi^2-1}$$
$$=0, \quad \text{antisymmetric wave.} \tag{7}$$

In Eqs. (6) and (7), $\xi=c_s/c$ is the ratio of shear wave velocity to the interface wave velocity, $\zeta=c_s/c_p$ is the ratio of the shear wave velocity to the compressional wave velocity, and $\bar{k}_1=(k_1/\omega)/z_s$ and $\bar{k}_2=(k_2/\omega)/z_s$ are the nondimensional fracture impedance ratios, where (k_i/ω) is the fracture impedance (fracture stiffness divided by the angular frequency) and z_s is the shear wave impedance (density multiplied by the shear wave velocity).

Equations (6) and (7) reveal that the velocities of the two interface waves are functions of the nondimensional fracture impedance ratios $\bar{k}_1$ and $\bar{k}_2$, and the Poisson's ratio of the half-spaces $v=0.5[(\zeta^{-2}-2)/(\zeta^{-2}-1)]$. Numerical solution of Eqs. (6) and (7) shows that with increasing the fracture impedance ratios, the velocities of the symmetric and antisymmetric interface waves increase from the Rayleigh wave velocity to the shear wave velocity.[5,6] The particle motions of both waves are elliptical retrograde near the fracture, reversing to prograde at less than a wavelength away from the fracture.

For the horizontal source configuration of Fig. 2(a), source–fracture symmetry requires that the shear stresses on the upper and lower surfaces vanish and the horizontal displacements on the upper and lower surfaces be equal,

$$\tau_{12}^a=\tau_{12}^b=0, \quad u_1^a=u_1^b. \tag{8}$$

Equations (8) reveal that the displacement–discontinuity boundary condition for the fracture, $u_1^b-u_1^a=\tau_{12}^a/k_1$, is always satisfied. This indicates that the tangential fracture stiffness has no effect on the symmetric fracture interface wave. Similarly, it can also be demonstrated that the normal fracture stiffness has no effect on the antisymmetric fracture interface wave (Fig. 3). The dependence of the symmetric and antisymmetric fracture interface waves on the fracture stiffness is consistent with that predicted by Eqs. (6) and (7).
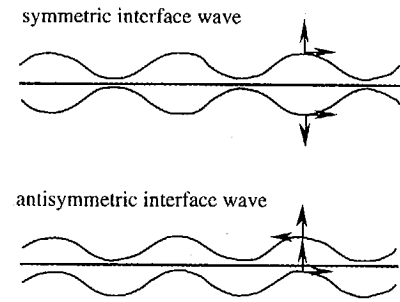
A. Effect of fracture stiffness

To evaluate the effects of fracture stiffness on fracture interface waves generated by a line source, a series of two-dimensional boundary element simulations were performed. The half-spaces were assigned properties typical of granite: compressional and shear wave velocities $c_p=5800$ m/s and $c_s=3800$ m/s, and density $\rho=2600$ kg/m^3. The two-dimensional fracture consisted of a line 76.0 m in length which was discretized into 100 quadratic elements. The source wavelet was a broadband three-loop wavelet with a central frequency of 800 Hz. The computation was carried out to 20.1 ms in 310 time steps.

Snapshots of the horizontal displacement at 10.37 ms are displayed for a completely welded fracture ($k_1=k_2=\infty$) and a nonwelded fracture ($k_2=5\times10^9$ Pa/m) in Figs. 4 and 5 for the two source configurations shown in Fig. 2. Figures 4 and 5 provide visual evidence that a compliant fracture concentrates wave energy along the fracture in the form of Rayleigh
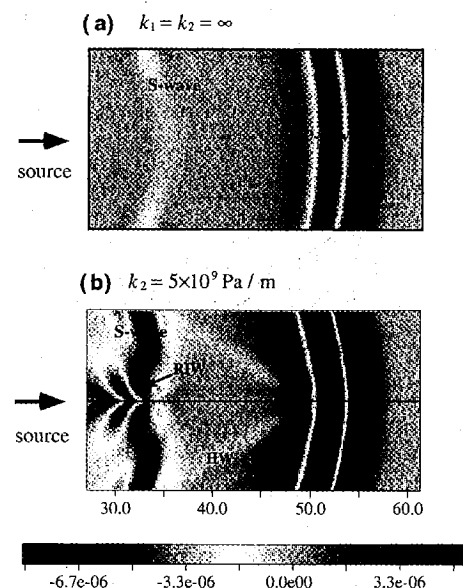

FIG. 4. Horizontal displacements near a fracture of (a) $k_1=k_2=\infty$ (an infinite space) and (b) $k_2=5\times10^9$ Pa/m for the source–fracture configuration shown in Fig. 2(a). A Rayleigh-type interface wave RIW and a head wave HW are present on the finite stiffness fracture in addition to the body compressional and shear waves.

(a) $k_1 = k_2 = \infty$

(b) $k_1 = 5 \times 10^9$ Pa / m

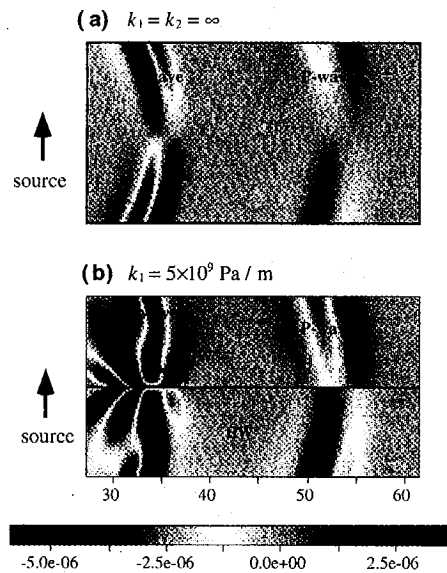-5.0e-06   -2.5e-06   0.0e+00   2.5e-06

FIG. 5. Horizontal displacements near a fracture of (a) $k_1 = k_2 = \infty$ (an infinite space) and (b) $k_1 = 5 \times 10^9$ Pa/m for the source–fracture configuration shown in Fig. 2(b). A Rayleigh-type interface wave RIW and a head wave HW are observed to exist on the finite stiffness fracture in addition to the body compressional and shear waves.

fracture interface waves (labeled RIW). A compliant fracture also supports a compressional head wave (labeled HW) which propagates along the fracture while continuously radiating energy into the half-spaces.

Particle displacement waveforms for a receiver located on the lower surface of the fracture at a distance of 45.79 m from the source are displayed for a range of fracture stiffnesses in Figs. 6 and 7 for the horizontally and vertically

(a) horizontal displacement

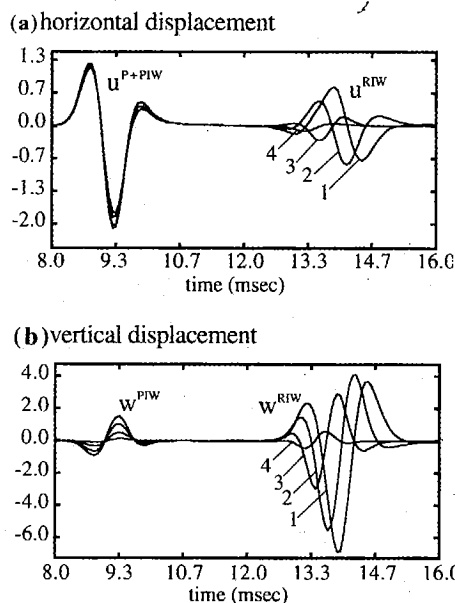
(b) vertical displacement

FIG. 6. Waveforms on the lower surface of the fracture at a distance of 45.79 m from the source for the model shown in Fig. 2(a). The fracture is assigned stiffness values of (1) $k_2 = 10^9$, (2) $k_2 = 5 \times 10^9$, (3) $k_2 = 2.5 \times 10^{10}$, and (4) $k_2 = 10^{11}$ Pa/m.

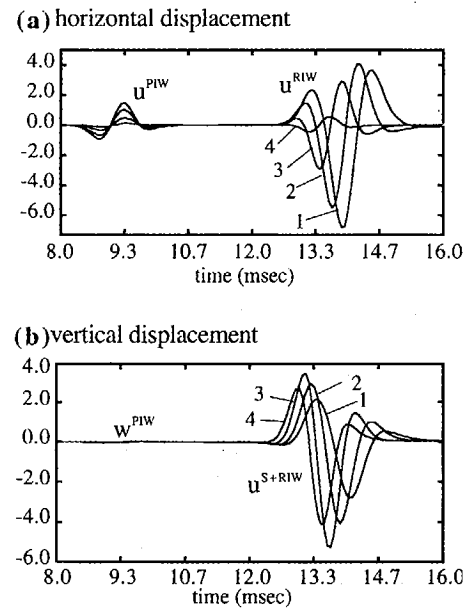**(a)** horizontal displacement

(b) vertical displacement

FIG. 7. Waveforms on the lower surface of the fracture at a distance of 45.79 m from the source for the simulation configuration shown in Fig. 2(b). The fracture is assigned stiffness values of (1) $k_1 = 5 \times 10^9$, (2) $k_1 = 10^{10}$, (3) $k_1 = 2.5 \times 10^{10}$, and (4) $k_1 = 10^{11}$ Pa/m.

polarized sources (Fig. 2). Four waves are present and are denoted by the superscripts PIW and RIW to indicate compressional and Rayleigh interface waves, P+PIW to denote a mixture of a compressional body wave and PIW, and S+RIW to denote a mixture of shear body wave and RIW. The mixing of RIW and the shear wave resulted because computational limitations prevented the use of a fracture long enough to allow the two waves to separate from each other.

A horizontally polarized source located on a welded fracture (i.e., whole space) produces only a compressional
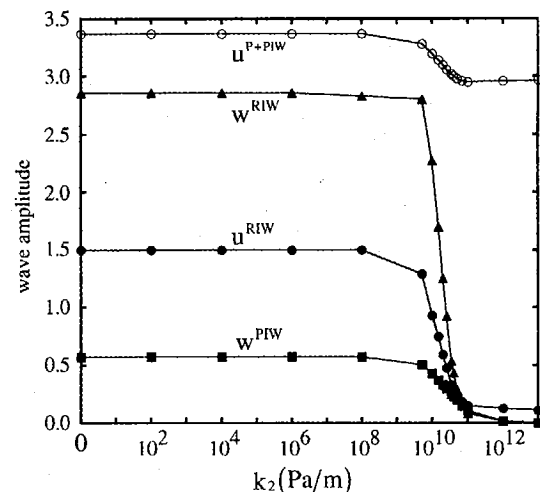

FIG. 8. Displacements on the fracture surface at a distance of 45.79 m from the source as a function of fracture stiffness for the model shown in Fig. 2(a).
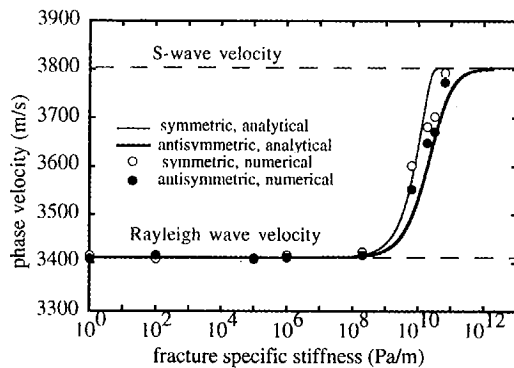
FIG. 9. Phase velocities of the symmetric and antisymmetric fracture interface waves as a function of fracture stiffness.

wave with horizontal displacement [Fig. 4(a)]. Therefore, w^{PIW}, u^{RIW}, and w^{RIW} shown in Figs. 4(a) and 6 exist solely due to the finite stiffness of the fracture, and hence are fracture interface waves. Because of the symmetry of the source–fracture configuration, w^{PIW}, u^{RIW}, and w^{RIW} must be symmetric about the fracture, that is, they are symmetric waves. Similarly, u^{PIW}, w^{PIW}, and u^{RIW} displayed in Figs. 5(b) and 7 for a vertically polarized source are antisymmetric about the fracture and are antisymmetric waves.

The displacements on the fracture surface, at a distance of 45.79 m from the source, are displayed in Fig. 8 as a function of fracture stiffnesses for a horizontally polarized source [Fig. 2(a)]. For the source spectrum and seismic properties of the half-spaces used in this simulation, a tangential fracture stiffness of $k_2 = 10^8$ Pa/m is the threshold value above which the displacements of all the waves traveling along the fracture start to decrease with increasing fracture stiffness. The decrease of u^{P+PIW}, $w^{PIW}_{,}$, u^{RIW}, and w^{RIW} results because the stiffness of the fracture is too large to result in localization of compressional and shear waves along the fracture. When the fracture stiffness increases above 10^{11} Pa/m (nearly welded condition), the small-amplitude u^{RIW} is the near-field term traveling directly from the source,[12] and the large-amplitude u^{P+PIW} is the compressional body wave.

The phase velocities of the symmetric and antisymmetric RIW interface waves are shown in Fig. 9 for a range of fracture stiffnesses. The analytic phase velocities were computed by numerical solution of the dispersion equations given in Eqs. (6) and (7). The numerical phase velocities were obtained from the RIW by calculating $L/(\Delta\Theta/\omega)$,

where L is the distance between two receiver locations 29.83 m and 44.65 m from the source, $\Delta\Theta$ is the phase difference between the interface waves at the two locations, and ω is the angular frequency. The phase velocities displayed in Fig. 9 indicate that the interface waves supported by a fracture are dispersive despite the zero thickness of the fracture. The numerical and analytic velocities show general agreement.

B. Effect of half-space impedance

To investigate the effects of the acoustic impedance of the half-spaces on fracture interface waves, a series of boundary element simulations were performed using the horizontal source [Fig. 2(a)] located on a 46.0-m-long fracture with a stiffness $k_2 = 10^9$ Pa/m. Both the upper and lower surfaces of the fracture were discretized into 201 nodes using 100 quadratic elements 0.46 m in length. The computation was carried out to 18.2 m in 460 time steps. The compressional wave impedance and density of the half-spaces are $z_p = 15\,080\,000$ m/s kg/m³ and $\rho = 2600$ kg/m³ while the shear wave impedance was varied from $z_s = 9\,880\,000$ to $z_s = 6\,634\,420$ m/s kg/m³, as listed in Table I. The compressional and shear wave velocities and Poisson's ratios calculated from z_p, z_s, and ρ are also given in Table I.

The waveforms recorded on the lower surface of the fracture at a distance of 23.12 m from the source are displayed in Fig. 10. u^{P+PIW}, w^{PIW}, u^{RIW}, and w^{RIW} waves have different shapes and amplitudes for different values of the shear wave impedance. Figure 11 displays the displacements as a function of the shear wave impedance. As z_s increases, interface waves w^{PIW}, u^{RIW}, and w^{RIW} increase, and u^{P+PIW} decreases. These variations in displacement indicate that more seismic energy is partitioned from the body wave part of u^{P+PIW} into w^{PIW}, u^{RIW}, and w^{RIW} with increasing z_s.

C. Particle motions

Particle motions recorded along a vertical profile [Fig. 2(a)] are displayed in Fig. 12. A horizontally polarized source was applied on the lower surface of the fracture with stiffnesses $k_1 = 5 \times 10^9$ and $k_2 = 10^9$ Pa/m. The particle motion of the S+RIW wave reverses from retrograde to prograde at a depth of $0.17\lambda_s$ (λ_s is the wavelength of the shear wave). The particle motion of the P+PIW wave reverses from prograde near the fracture to retrograde at a depth of $0.17\lambda_p$ (λ_p indicates the wavelength of the compressional wave). The vertical component of the P+PIW wave and the horizontal component of the S+RIW wave pass through zero

TABLE I. Properties of the half-spaces.

z_P m/s kg/m³	z_S m/s kg/m³	ρ · kg/m³	C_P m/s	C_S m/s	v
15 080 000	9 880 000	2 600	5 800	3 800.0	0.12
15 080 000	9 508 720	2 600	5 800	3 657.2	0.17
15 080 000	9 035 000	2 600	5 800	3 475.0	0.22
15 080 000	8 464 560	2 600	5 800	3 255.6	0.27
15 080 000	7 596 160	2 600	5 800	2 921.6	0.33
15 080 000	6 634 420	2 600	5 800	2 551.7	0.38

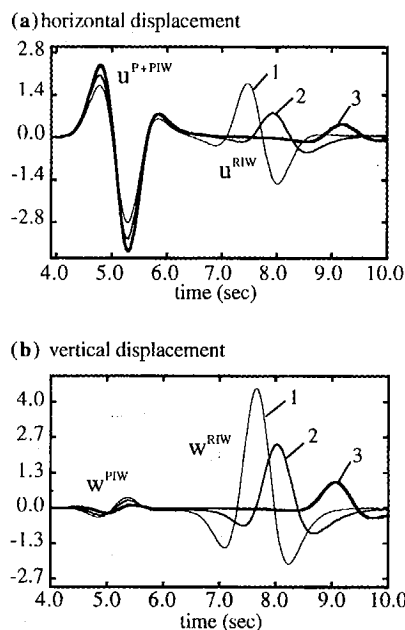(a) horizontal displacement

(b) vertical displacement

FIG. 10. Waveforms on the lower fracture surface at a distance of 23.12 m from the source for the model shown in Fig. 2(a). The fracture stiffness is $k_2 = 10^9$ Pa/m, the compressional wave impedance is $z_P = 15\,080\,000$ m/s kg/m³, and the shear wave impedance is: (1) $z_S = 9\,880\,000$, (2) $z_S = 9\,035\,000$, and (3) $z_S = 7\,596\,160$ m/s kg/m³.

at depths of $0.17\lambda_p$ and $0.17\lambda_s$, respectively. The vertical displacement of the P+PIW wave reaches a maximum at approximately $0.06\lambda_p$ away from the fracture. Figure 12 also displays particle motions of the P+PIW and S+RIW waves which become less elliptically and more linearly polarized at depths greater than $1.18\lambda_s$, and particle trajectories that are smaller on the upper half-space than the lower half-space.

Elliptical particle motions which decay exponentially away from the fracture while changing from retrograde to prograde are characteristic of Rayleigh fracture interface waves,[5,6] which can be viewed as stiffness-coupled free-surface Rayleigh waves on the upper and lower fracture surfaces. The particle motions of Fig. 12 indicate that fracture
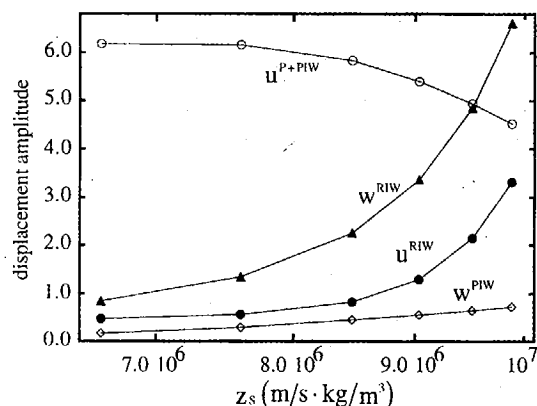

FIG. 11. Displacements on the fracture surface at a distance of 23.12 m from the source as a function of the shear wave impedance of the halfspaces for the simulation configuration shown in Fig. 2(a).
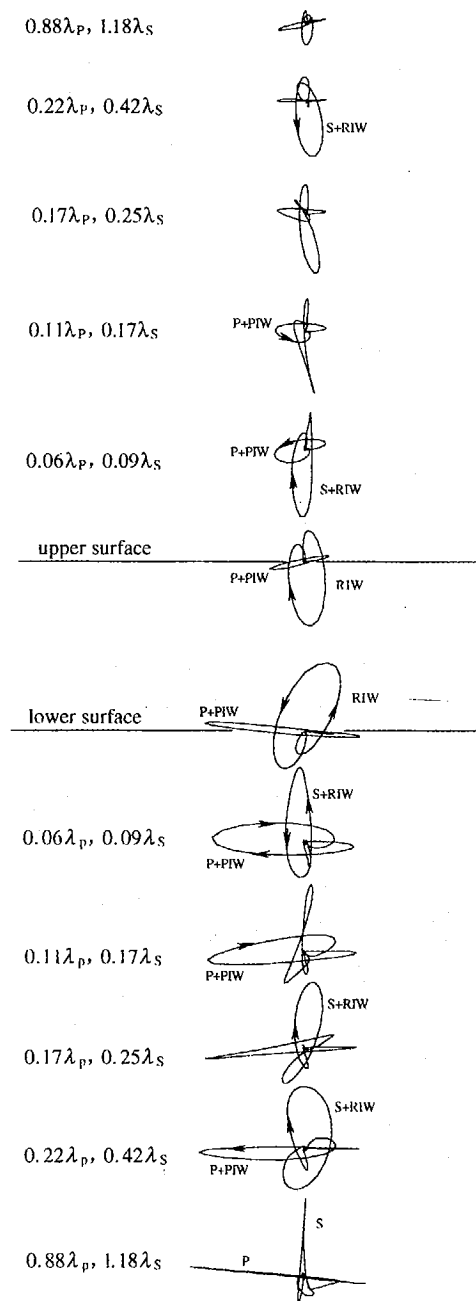

FIG. 12. Particle motions of waves recorded along the vertical profile in Fig. 2(a). The fracture stiffnesses are $k_1 = 10^9$ and $k_2 = 5 \times 10^9$ Pa/m.

interface waves are localized to within $1.2\lambda_s$ of the fracture, and that beyond this depth compressional and shear body waves dominate. Smaller particle trajectories in the upper half-space results because seismic energy is not completely transmitted from the lower half-space to the upper half-space because of the finite stiffness of the fracture. The particle motion of the PIW interface wave is consistent with that of water surface waves on water.

D. Generation by an off-fracture source

The effects of source depth on the generation of fracture interface waves is examined using the model geometry shown in Fig. 13 (see Table II). The 76.0-m-long fracture
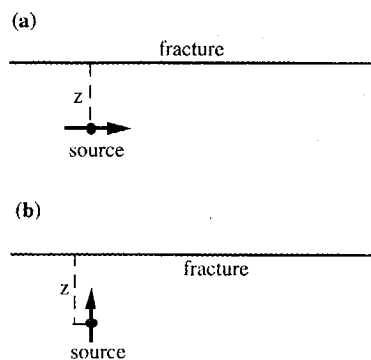
(a)

fracture

z

source

(b)

fracture

z

source

FIG. 13. Model used to examine the effects of source depth on the generation of fracture interface waves.
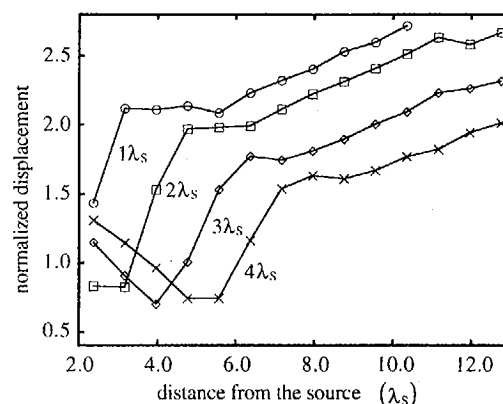

FIG. 14. Normalized horizontal displacements of the RIW interface wave on the lower fracture surface as a function of distance from the source along the fracture for the model shown in Fig. 13(a). The numbers labeled on the curves are the source depths. Symbol λ_s denotes the shear wave wavelength.

was assigned stiffnesses of $k_1 = k_2 = 2.5 \times 10^{10}$ Pa/m. The two half-spaces were assigned compressional and shear wave velocities $c_p = 5800$ m/s and $c_s = 3800$ m/s, and a density $\rho = 2600$ kg/m^3. The fracture was discretized into 100 quadratic elements, and the computation was carried out to 20.1 ms in 310 time steps. The source depth was varied from $1\lambda_s$ to $4\lambda_s$.

Because of the geometric spreading, body waves at the fracture become smaller as the source moves deeper. The variation of the incidence body wave will produce changes in amplitude of the generated interface waves. In the analysis, the fracture interface waves recorded on the fracture surfaces are normalized by the amplitude of the incidence body wave. Figure 14 displays normalized horizontal displacements of the RIW interface wave recorded on the lower fracture surface as a function of distance from the source along the fracture for the simulation configuration shown in Fig. 13(a). The numbers labeled on the curves are source depths in terms of shear wave wavelengths.

For discussion convenience, the curve for source depth $z = 3\lambda_s$ in Fig. 14 is replotted in Fig. 15. The variation of the normalized displacement can be explained as follows. From E and A, the main mechanism is the reflection of the incident body wave. The reflected wave decreases with increasing incidence angle θ. At location A, a critical incidence angle for the generation of the RIW interface wave is reached. As the wave travels from A to B, the RIW interface wave is developing, resulting in a continuous increase of the RIW interface wave. After location B, the persisting but slower increase of the normalized displacement with propagation distance may be due to the decrease of the incident body wave instead of the growth of the RIW interface wave. In other words, the RIW interface wave may be already fully developed at point B.

The angle θ defined in Fig. 15 are listed in Tables II and III for the horizontally and vertically polarized sources, re-

spectively [see Fig. 13(a) and (b)]. It is found from Tables II and III that as source depth increases from $1\lambda_s$ to $4\lambda_s$, and θ decreases from around 72.5 to 63 degrees.

III. SUMMARY AND CONCLUSIONS

This paper has used boundary element simulations to examine the properties of fracture interface waves generated by a line source located near a single fracture. The fracture was modeled as a displacement–discontinuity boundary condition between two elastic half-spaces. The effects of fracture stiffness and the seismic impedance of the half-spaces on the fracture interface waves and the influences of the source depth on the generation of the fracture interface waves were examined.

The numerical simulations reveal that symmetric and antisymmetric Rayleigh fracture interface waves can be generated by a directional source located on or near the fracture and polarized in the tangential and orthogonal directions with respect to the fracture, respectively. The symmetric interface wave is supported by the normal fracture stiffness, and the antisymmetric fracture interface wave is supported by the tangential fracture stiffness. The velocity and ampli-
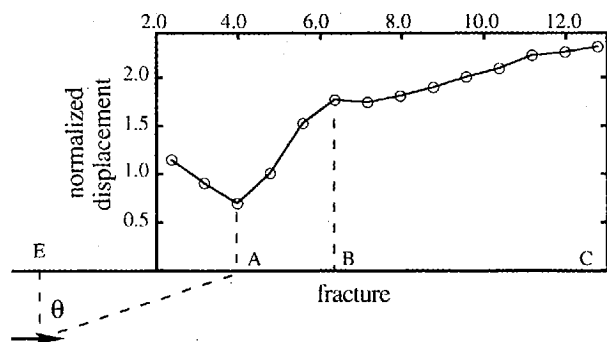
TABLE II. Critical angles for the generation of the Rayleigh fracture interface waves (RIW) for the source–fracture configuration shown in Fig. 13(a).

Source depth (λ_s)	1	2	3	4
θ (degree)	72.6	67.4	64.9	63.4

FIG. 15. Normalized displacement on the fracture surface as a function of the critical angle θ for the generation of RIW interface waves.

TABLE III. Critical angles for the generation of RIW interface waves for the source-fracture configuration shown in Fig. 13(b).

Source depth (λ_s)	1	2	3	4
θ (degree)	72.4	67.2	64.7	63.3

tude of the interface waves are functions of the ratio of the fracture impedance to the half-space impedance. There is a threshold value of the fracture stiffness above which the fracture interface waves start to decrease in amplitude with increasing fracture stiffness. The interface waves also increase as the shear wave acoustic impedance increases. With increasing fracture stiffness from the threshold to infinity, the phase velocity of the RIW interface waves increase from the free-surface Rayleigh wave velocity to the shear wave velocity. The symmetric interface wave propagates faster than the antisymmetric interface wave for a given value of the fracture stiffness and the half-space impedance.

The PIW and RIW waves exhibit elliptical particle motion because of the existence of a phase shift between two displacement components. Particle motion ellipse of the PIW wave is polarized largely in the horizontal direction while that of the RIW wave is polarized more vertically than horizontally. The direction of the particle motion of the RIW wave is retrograde near the fracture and reverses to prograde at a depth of less than a wavelength, while the particle motion of the PIW wave changes from prograde near the fracture to retrograde. The particle motion of the PIW and RIW interface waves are consistent, respectively, with that of water surface waves and the free-surface Rayleigh wave. In addition to the two fracture interface waves, a head wave is also observed to exist on a finite stiffness fracture.

These results may find direct applications to seismic detection and characterization of fractures in the rock. For example, the leaky nature of the fracture head wave may allow fractures to be detected by receivers located off the fracture. The sensitivities of the symmetric and antisymmetric interface waves to the normal and tangential fracture stiffnesses, respectively, may allow separate estimates of these properties from the velocities of fracture interface waves.

ACKNOWLEDGMENTS

[1] K. Kendall and D. Tabor, "An ultrasonic study of the area of contact between stationary and sliding surfaces," Proc. R. Soc. London, Ser. A **323**, 321–340 (1971).

[2] M. Schoenberg, "Elastic wave behavior across linear slip interfaces," J. Acoust. Soc. Am. **68**, 1516–1521 (1980).

[3] L. J. Pyrak-Nolte, L. R. Myer, and N. G. W. Cook, "Transmission of seismic waves across natural fractures," J. Geophys. Res. **95**, 8617–8638 (1990).

[4] S. I. Rokhlin and Y. J. Wang, "Analysis of boundary conditions for elastic wave interaction with an interface between two solids," J. Acoust. Soc. Am. **89**, 503–515 (1991).

[5] B. Gu, K. T. Nihei, and L. R. Myer, "Fracture interface waves," J. Geophys. Res. **101**, 827–835 (1996).

[6] L. J. Pyrak-Nolte and N. G. W. Cook, "Elastic interface waves along a fracture," Geophys. Res. Lett. **14**, 1107–1110 (1987).

[7] G. S. Murty, "A theoretical model for the attenuation and dispersion of Stoneley waves at the loosely bonded interface of an elastic half-space," Phys. Earth Planet. Interiors **11**, 65–79 (1975).

[8] L. J. Pyrak-Nolte, J. Xu, and G. M. Haley, "Elastic interface waves propagating in a fracture," Phys. Rev. Lett. **68**, 3650–3653 (1992).

[9] P. B. Nagy and L. Adler, "New ultrasonic techniques to evaluate interfaces," in *Elastic Waves and Ultrasonic Nondestructive Evaluation*, edited by A. K. Datta, J. D. Achenbach, and Y. J. Rajapaske (North-Holland, New York, 1990), pp. 229–239.

[10] B. Gu, K. T. Nihei, L. R. Myer, and L. J. Pyrak-Nolte, "Numerical simulation of elastic wave propagation in fractured rock with the boundary integral equation method," J. Geophys. Res. **101**, 15 933–15 943 (1996).

[11] G. D. Manolis and D. E. Beskos, *Boundary Element Methods in Elastodynamics* (Unwin Hyman, Boston, 1988).

[12] K. Aki and P. G. Richards, *Quantitative Seismology* (Freeman, New York, 1980), Vol. 1, p. 87.

127   J. Acoust. Soc. Am., Vol. 102, No. 1, July 1997

Gu *et al.*: Fracture interface waves   127